

## Grain size dependent deformation microstructure evolution and work-hardening in CoCrNi medium entropy alloy

Shuhei Yoshida<sup>a,\*</sup>, Genki Yamashita<sup>a</sup>, Takuto Ikeuchi<sup>a</sup>, Yu Bai<sup>b</sup>, Akinobu Shibata<sup>c</sup>, Nobuhiro Tsuji<sup>a</sup>

<sup>a</sup> Department of Materials Science and Engineering, Kyoto University, Kyoto, Japan

<sup>b</sup> School of Materials Science and Engineering, Dalian University of Technology, Dalian, China

<sup>c</sup> Research Center for Structural Materials, National Institute for Materials Science, Tsukuba, Japan

### ARTICLE INFO

#### Keywords:

Ultrafine-grained metals  
High/medium entropy alloys  
Deformation microstructure  
Deformation twins  
Grain boundary-mediated plasticity

### ABSTRACT

This study clarified the grain size dependence of the deformation microstructure evolution and work-hardening behavior in CoCrNi medium entropy alloy. We fabricated fully recrystallized specimens with coarse-grained (CG) and ultrafine-grained (UFG) specimens by severe plastic deformation and subsequent annealing processes. Tensile deformation was applied to the specimens at room temperature. The UFG specimen exhibited both high strength and high ductility compared to conventional UFG metals due to the high work-hardening ability. In the CG specimen, three distinct types of deformation microstructures consisting of dislocations and deformation twins developed depending on grain orientations, similar to the single-crystalline specimens. In the UFG specimen, widely-extended stacking faults and randomly-tangled dislocations were found to coexist in most grains. Deformation twins were found to nucleate without evidence of dislocation reactions regardless of grain orientations, implying abnormal nucleation mechanisms of deformation twins in the UFG specimen. Dislocation densities quantified by in-situ synchrotron XRD measurements during tensile deformation were higher in the UFG specimen than those in the CG specimen and conventional UFG metals. Our analysis showed that the work-hardening behavior of the specimens was primarily controlled by increases in dislocation density as well as the introduction of planar defects during deformation. Through comparisons with the CG specimen and conventional UFG metals, we concluded that the excellent work-hardening ability of the UFG specimen was mainly due to the evolution of unique deformation microstructures and rapid increase in dislocation density, which could be due to inhibited dynamic recovery in the MEA.

### 1. Introduction

Structural metallic materials are indispensable for ensuring the safety and stability of our daily life and supporting social infrastructure, such as vehicles and buildings. These materials are often required to possess both high strength and also high ductility. However, there is typically a trade-off relationship between the strength and ductility of materials, making it challenging to achieve both simultaneously. For instance, ultra-fine grain (UFG) metals or nanostructured metals [1–3] with a mean grain size of less than 1  $\mu\text{m}$ , fabricated by severe plastic deformation (SPD) [4–6] (and subsequent short-term annealing), have been reported to exhibit significantly high strength due to grain refinement strengthening. Tsuji et al. [7] reported that the yield strength of 1100 commercial purity aluminum and interstitial-free steel

increased about four times after accumulative roll bonding process, an SPD process, due to grain refinement. Nevertheless, their ductility is typically limited to only a few percent. This limitation can be understood by Considère's criterion [8] for plastic instability, which is expressed as:

$$\frac{d\sigma}{d\varepsilon} < \sigma, \quad (1)$$

where  $\sigma$  and  $\varepsilon$  are the true stress and true strain of materials deformed by uniaxial tension. When the work-hardening rate,  $\frac{d\sigma}{d\varepsilon}$ , becomes smaller than the flow stress, macroscopic necking occurs in the gauge part of tensile specimens, followed by fracture. Since the strength of UFG metals is very high, plastic instability tends to occur at an early stage of deformation, resulting in limited ductility. Therefore, a high work-

\* Corresponding author.

E-mail address: [yoshida.shuhei.5s@kyoto-u.ac.jp](mailto:yoshida.shuhei.5s@kyoto-u.ac.jp) (S. Yoshida).

<https://doi.org/10.1016/j.jalms.2024.100123>

Received 30 August 2024; Received in revised form 18 October 2024; Accepted 31 October 2024

Available online 3 November 2024

2949-9178/© 2024 The Author(s). Published by Elsevier B.V. This is an open access article under the CC BY license (<http://creativecommons.org/licenses/by/4.0/>).

hardening rate is necessary to delay necking and enhance the ductility of UFG metals with high strength.

Interestingly, some face-centered cubic (FCC) alloys with fully recrystallized UFG microstructure have been reported to exhibit distinctive mechanical properties, achieving high strength and high ductility simultaneously [9–15]. For example, Saha et al. [9] reported that a high Mn steel with fully recrystallized ultrafine grain microstructures exhibited high yield strength and high ductility. Also, in our previous study [11], we successfully fabricated equiatomic CoCrNi medium entropy alloy (MEA) with fully recrystallized microstructure and a wide range of average grain sizes ( $10^2$ – $10^{-1}$   $\mu\text{m}$ ) through high-pressure torsion (HPT) [16], one of the SPD processes, and subsequent annealing. We found that the strength of the MEA substantially increased as the grain size decreased to the UFG regime, while the ductility was still maintained due to its high work-hardening ability. Similar mechanical behaviors have also been reported in UFG materials with different crystal structures [17,18]. We suppose that this unique work-hardening behavior might be due to the activation of unusual deformation mechanisms or the evolution of abnormal deformation microstructures. However, due to the lack of systematic investigation of deformation microstructures, the exact reason responsible for the exceptional mechanical properties of the CoCrNi MEA with UFG microstructure has remained elusive.

Therefore, in order to clarify the characteristics of deformation microstructures and the microstructural origin of the high work-hardening ability in equiatomic CoCrNi MEA with fully recrystallized UFG microstructure, we systematically investigated the grain size dependence on the evolution of deformation microstructures in CoCrNi MEA and the influence on the macroscopic work-hardening behavior. Through systematic and detailed comparison between coarse-grained (CG) and UFG specimens of the CoCrNi MEA as well as conventional UFG metals, we will discuss the essential characteristics of deformation microstructures and work-hardening in UFG metals and alloys.

## 2. Materials and methods

### 2.1. Materials fabrication and processing

Button-shaped ingots with a thickness of approximately 10 mm and a diameter of approximately 25 mm were synthesized by vacuum arc melting of high-purity cobalt, chromium, and nickel (purity greater than 99.9 wt%) under an argon atmosphere. The ingots were remelted five times to achieve a uniform distribution of elements. The ingots were then cold rolled to a thickness of 3.6 mm, a reduction of approximately 64 %. These cold-rolled specimens were then homogenized in a vacuum furnace at a temperature of 1100 °C for 18 h, followed by rapid quenching in water. A second cycle of cold rolling further reduced the specimen thickness to 1.0 mm (equivalent to a 72 % reduction), after which the specimens were annealed at 1100 °C for 24 h followed by water quenching.

Disk specimens with a diameter of 10 mm and a thickness of 0.8 mm, cut from the materials after the processes above, were subjected to high-pressure torsion (HPT) for five rotations, corresponding to a maximum shear strain of 196, at a compressive stress of 6 GPa and a rotational speed of 0.2 revolutions per minute at room temperature. After HPT, the materials were annealed at 1100 °C for 1.8 ks and at 850 °C for 120 s followed by water quenching to obtain CG and UFG specimens, respectively, with fully recrystallized microstructures.

### 2.2. Mechanical testing

Tensile tests were performed at room temperature with an initial strain rate of  $8.3 \times 10^{-4} \text{ s}^{-1}$  using a precision universal mechanical testing machine. Tensile specimens, with the gauge dimensions of 2.0 mm in length, 1.0 mm in width, and 0.5 mm in thickness, were cut from the HPT disks by wire electrical discharge machining. To facilitate

strain distribution analysis, the specimen surfaces were painted with a stochastic pattern of black and white ink. The displacement of these patterns during tensile deformation was monitored by a charge-coupled device (CCD) camera, capturing images at a rate of 5.0 frames per second. The strain distribution in the gage part of the specimen was quantified using the digital image correlation (DIC) technique [19]. This method with small-sized tensile specimens has been validated to provide stress-strain curves comparable to those derived from standard-sized specimens [11,20,21].

### 2.3. Microstructure characterization

Microstructural characterization, both before and after tensile deformation, was performed using scanning electron microscopy (SEM) and (scanning) transmission electron microscopy ((S)TEM). It should be noted that, in our study, we prepared different specimens tensile-deformed to different strains, and the part near half the specimen thickness was used for microscopy observations. This is because deformation microstructures near the surface of specimens may be different from the inner part due to different constraint conditions. In each deformation condition, more than 20 grains in two SEM specimens and two TEM specimens were observed to ensure the statistical reliability of the results.

Prior to SEM analysis, the surface of the tensile specimens (corresponding to the HPT disk surface) was mechanically polished, followed by electropolishing in an electrolyte of 10 vol% perchloric acid and 90 vol% ethanol at a voltage of 30 V for 15 s at room temperature to achieve a mirror-like surface. SEM observations were performed using a JSM-7100F/7800 F (JEOL Ltd.) equipped with a backscattered electron detector and electron backscattering diffraction detector. Electron channeling contrast imaging (ECCI) was used to delineate the distribution of lattice defects at an acceleration voltage of 25 kV, a probe current of 1 nA, and a working distance of 3.0 mm. The crystal orientation of the grains observed by SEM-ECCI was evaluated by SEM-EBSD at an acceleration voltage of 15 kV, a probe current of 1 nA, and a working distance of 15.0 mm.

For TEM analysis, the surface specimens (the same section used for the SEM observations) were first mechanically thinned to a thickness of 100  $\mu\text{m}$  and then further polished by twin-jet electropolishing using Tenupol-5 (Struers Ltd.) in an electrolyte composed of 10 vol% perchloric acid, 20 vol% glycerin, and 70 vol% methanol at 15 V and 243 K. (S)TEM observations were performed with a JEM-2100F (JEOL Ltd.) equipped with bright field and annular dark field detectors for STEM, operated at an acceleration voltage of 200 kV. Lattice defects in the deformed specimens were visualized by diffraction contrast in both TEM and STEM, and by phase contrast in TEM. The grain orientations of the observed areas were deduced from the convergent beam electron diffraction (CBED) patterns (Kikuchi patterns).

### 2.4. In-situ X-ray diffraction (XRD) measurements during tensile deformation

Time-resolved in-situ synchrotron XRD measurements during tensile deformation were performed at a synchrotron facility, the beamline No. 46XU of Super Photon ring – 8 GeV (Spring-8) with an undulator X-ray source. Tensile specimens with the same dimensions as used in 2.2 were mounted to a homemade tensile test machine placed on a computer-controlled four-axis goniometer, and tensile deformation was applied with a quasi-static strain rate of  $8.3 \times 10^{-4} \text{ s}^{-1}$  at room temperature. Monochromated incident X-ray beam with the energy of 30 keV (wavelength:  $\lambda = 0.0413 \text{ nm}$ ) was irradiated at the center of the gauge part of the tensile specimens. Transmitted diffraction signals of X-ray were collected by one-dimensional high-resolution X-ray detectors where six MYTHEN detectors (DECTRIS AG) were serially connected. The detection system was calibrated by using a well-annealed CeO<sub>2</sub> standard sample. The diffraction profiles were continuously collected

with the acquisition rate of 1.0 frame (profile) per second.

The diffraction profiles were analyzed by the convolutional multiple whole profile (CMWP) fitting method to obtain dislocation densities and planar fault probabilities (an indicator showing the abundance of intrinsic stacking faults) of the specimens during tensile deformation. In the analysis, diffraction peaks of  $\{hkl\} = \{111, 200, 220, 311, 222\}$  were used. The experimental diffraction profiles were fitted by theoretical models considering the effects of crystallite size, its statistical distribution, dislocation density, character of dislocations, and stacking faults. For the details of the theory, readers can refer to Ref. [22]. It should be noted that, due to the small diffraction angle ( $2\theta$ ), the diffraction signals are considered to be coming from grains with the tensile axis nearly parallel to  $\langle hkl \rangle$ .

### 3. Results

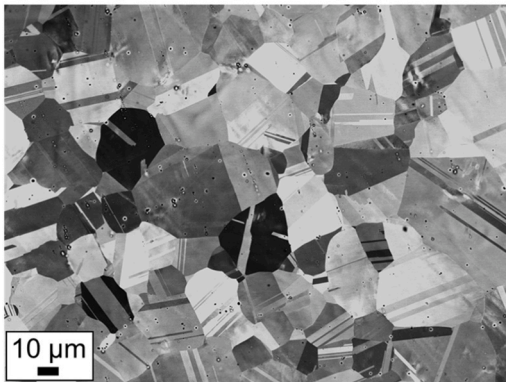
#### 3.1. Initial microstructure of the CG and UFG specimens

Fig. 1 (a) and (b) show the microstructures of the CG and UFG specimens before tensile deformation, fabricated by HPT and subsequent annealing. In both specimens, fully recrystallized equiaxed microstructures with many annealing twins were obtained. The numerous annealing twins are possibly attributed to the low stacking fault energy (SFE) of this MEA, reported as  $15 \sim 25 \text{ mJm}^{-2}$  [23,24]. The average grain sizes (including annealing twin boundaries) of the CG and UFG specimens determined by the line intercept method were  $9.3 \pm 1.91 \mu\text{m}$  and  $0.40 \pm 0.090 \mu\text{m}$ , respectively.

#### 3.2. Mechanical properties of the CG and UFG specimens

Fig. 2 (a) displays the nominal stress - nominal strain curves for the

(a) CG specimen ( $d = 9.3 \mu\text{m}$ )



(b) UFG specimen ( $d = 0.40 \mu\text{m}$ )

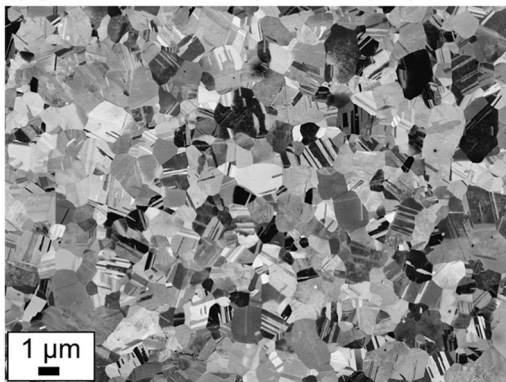


Fig. 1. Microstructures of the (a) CG and (b) UFG specimens before tensile deformation. The average grain sizes (including annealing twin boundaries) of the specimens are indicated in the figure.

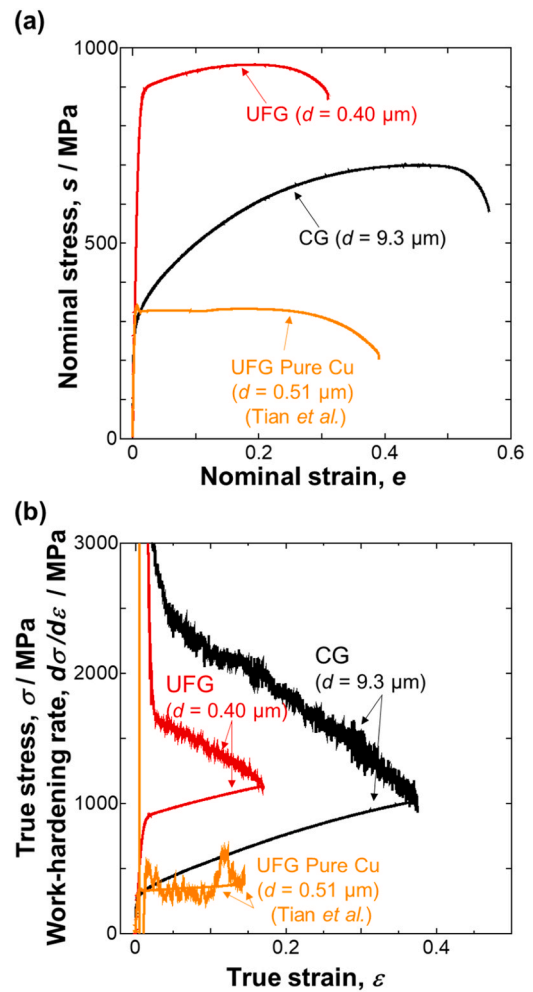


Fig. 2. (a) Nominal stress - nominal strain curves and (b) true stress - true strain and work-hardening rate - true strain curves of the CG and UFG specimens obtained by tensile tests at room temperature. The data of pure Cu with a fully recrystallized UFG microstructure (grain size of  $d = 0.51 \mu\text{m}$ ) extracted from literature [25] is also plotted as a reference. The portions of the curves after necking are not shown in (b).

CG and UFG specimens obtained from tensile tests conducted at room temperature. In the figure, the data of a pure Cu with a fully recrystallized UFG microstructure (grain size of  $d = 0.51 \mu\text{m}$ ), extracted from literature [25] is also plotted together as a reference. The CG specimen exhibited a yield strength of 240 MPa, an ultimate tensile strength of 710 MPa, a uniform elongation of 43 %, and a total elongation of 58 %. In contrast, the UFG specimen showed a yield strength of 760 MPa, an ultimate tensile strength of 950 MPa, a uniform elongation of 17 %, and a total elongation of 33 %. Although the Young's modulus is 1.73 times higher in the MEA (226 GPa) than pure Cu (130 GPa) [11], the UFG specimen of the MEA exhibited 2.3 times higher yield strength and 2.8 times higher ultimate tensile strength while their ductility is comparable (i.e., superior strength-ductility balance in the UFG specimen of the MEA). We also note that the yield strength of the UFG specimen (760 MPa) was about 140 MPa higher than the value estimated by the Hall-Petch relationship for coarse grain size regions reported in our previous studies [11,26]. This is presumably because the so-called extra-hardening effect, which is commonly observed in fully recrystallized UFG materials [11,12,20,27,28], owing to the lack of mobile dislocations in each grain and generation of lattice defects from grain boundaries (as discussed later). Fig. 2(b) shows the true stress-true strain curves and work-hardening rate-true strain curves for the CG and UFG specimens. Both specimens exhibited a monotonic decrease in

work-hardening rate with increasing strain. For the CG specimen, the slope of the work-hardening rate curve gradually decreased after a true strain of approximately 0.05. The plastic instability condition (Eq. (1)) was fulfilled immediately prior to fracture. On the other hand, the UFG specimen exhibited a pronounced decrease in the slope of the work-hardening rate at a true strain of approximately 0.03, followed by significant post-uniform elongation upon satisfying the plastic instability condition (Eq. (1)). However, the work-hardening rate of the UFG specimen was much higher than the curve of the pure Cu and other conventional UFG metals, in which work-hardening capacity is rapidly consumed, reported in literature, leading to better strength-ductility balance of the UFG specimen of the MEA.

### 3.3. Deformation microstructure evolution in the CG and UFG specimens

To better comprehend the deformation behavior of the CG and UFG specimens, we observed the deformation microstructure of the specimens, that were tensile-deformed to different strains, by using SEM-ECCI and (S)TEM.

#### 3.3.1. Deformation microstructures of the CG specimen

Fig. 3 summarizes the deformation microstructures observed in the CG specimen. There are three distinct types of microstructures: Type A (Fig. 3 (a-c)), Type B (Fig. 3 (d-f)), and Type B + T (Fig. 3 (g, h)). Type A microstructures exhibit an initial formation of randomly tangled dislocations after yielding (Fig. 3 (a)). With increasing strains ( $e \sim 5\%$  (Fig. 3 (b)) and  $15\%$  (Fig. 3 (c))), these dislocations progressively coalesce into dislocation cells (DCs) with the sizes of smaller than 100 nm. Type B microstructures demonstrate a clear piling-up of dislocations along specific  $\{1\ 1\ 1\}$  planes near grain boundaries at the onset of yielding (Fig. 3 (d)). This is then followed by a significant increase in dislocation

density within these specific  $\{1\ 1\ 1\}$  planes, ultimately resulting in the formation of planar dislocation structures (PDSs) (Fig. 3 (e, f)). Type B + T grains exhibit type B microstructure together with exceptionally fine deformation twins after an applied strain of  $5\%$  (Fig. 3 (g, h)), with their thicknesses (intervals) of several tens of nanometers. It should be noted that we differentiate these deformation twins from annealing twins, which are typically one to two orders of magnitude thicker. We also noticed that the number of the variants of the deformation twins in the CG specimen is two in most of type B + T grains. Fig. 6 (a) presents the tensile axis orientation of grains exhibiting these different microstructural types at an applied strain of  $5\%$ . Type A microstructures predominantly form in grains aligned near  $\langle 1\ 0\ 0 \rangle$ , whereas Type B microstructures emerge in grains of other orientations. Furthermore, Type B + T microstructures are prevalently observed in grains oriented near  $\langle 1\ 1\ 1 \rangle$ .

#### 3.3.2. Deformation microstructures of the UFG specimen

In the UFG specimen, deformation microstructures distinct from the case of the CG specimen were observed, as summarized in Fig. 4. Upon yielding ( $e \sim 0.9\%$ ), only grains with randomly tangled dislocations and widely extended stacking faults coexisting, categorized as type C microstructure, could be found (Fig. 4 (a)). After a nominal strain of  $e \sim 5\%$ , the density of both dislocations and widely-extended stacking faults increased (Fig. 4 (b, c)). In addition, in some grains (categorized as type C + T), a straight lamellae morphology was observed (Fig. 4 (d)). To clarify the details, these lamellae parts were magnified, and the phase contrast (lattice image) was obtained using TEM. Fig. 5 (a) and (b) show the lattice image of the lamellae morphology and the corresponding fast Fourier transformed (FFT) image, respectively. These images reveal that the lamellae morphology corresponds to very thin deformation twins with thicknesses of less than 10 nm, approximately. Fig. 6 (b) displays

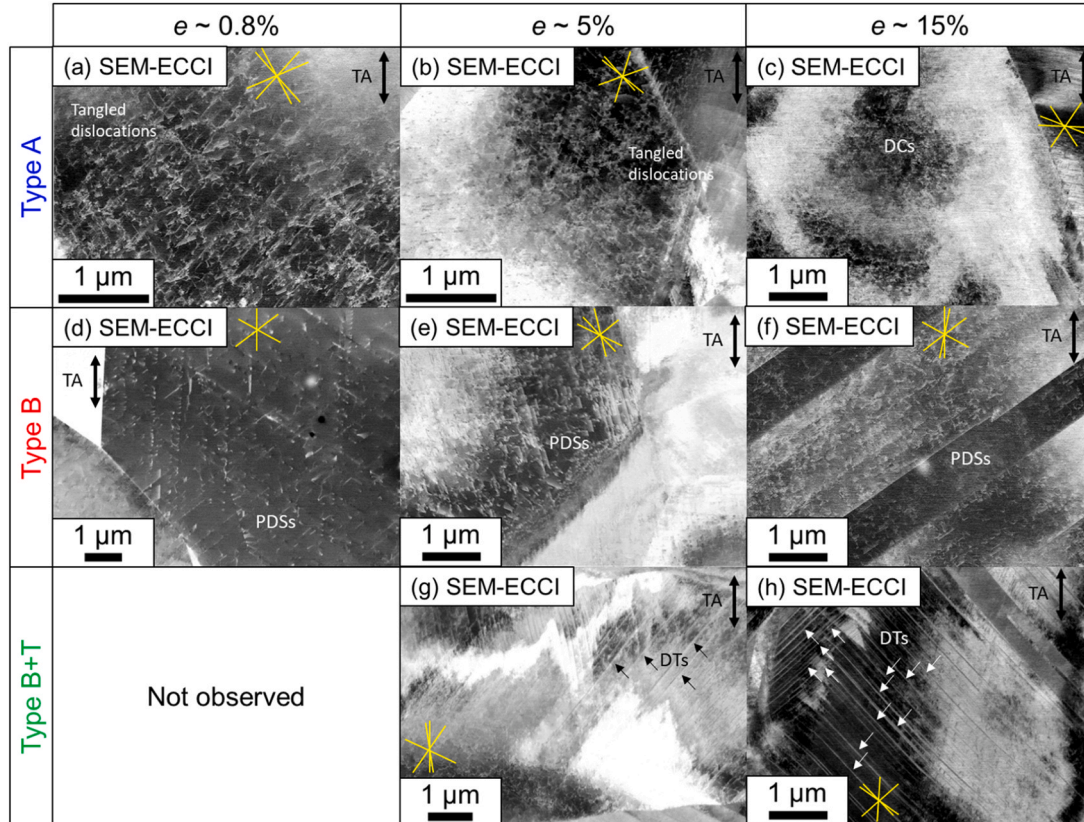
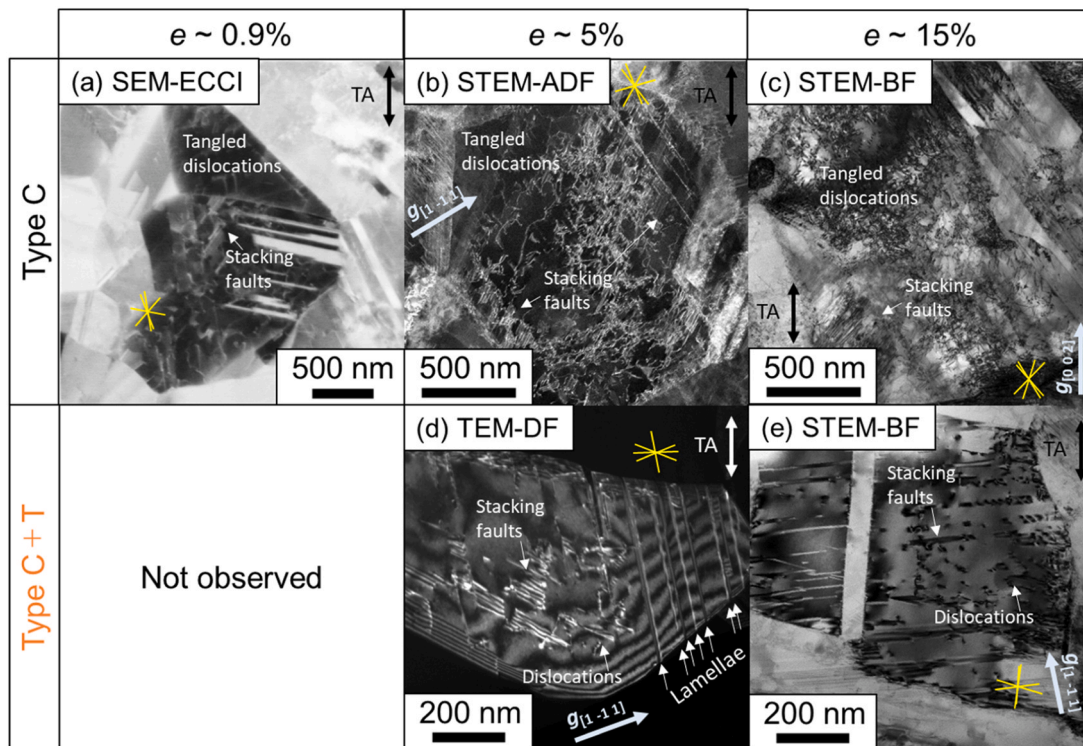
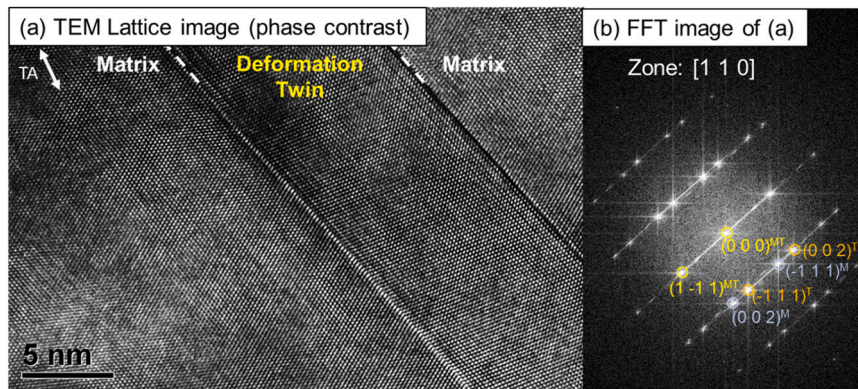


Fig. 3. Deformation microstructures of the CG specimen with three types (Type A, B, B + T) at strains of  $e \sim$  (a, d) 0.8, (b, e, g) 5.0, (c, f, h) 15%. Tensile directions and traces of  $\{1\ 1\ 1\}$  planes of an FCC structure are indicated by arrows and solid lines, respectively, in the figures. Type B + T microstructure at a strain of  $e \sim 0.8\%$  was not observed.



**Fig. 4.** Deformation microstructures of the UFG specimen with two types (Type C and C + T) at strains of  $e \sim$  (a) 0.9, (b) 5.0, and (c) 15%. Tensile directions and traces of  $\{1\ 1\ 1\}$  planes of an FCC structure are indicated by arrows and solid lines, respectively, in the figures. For the STEM-ADF (b), BF (c, e), and TEM dark-field (DF) (d) images,  $g$ -vectors used for the diffraction contrast imaging are also indicated. Type C + T microstructure at a strain of  $e \sim 0.9\%$  was not observed.



**Fig. 5.** (a) Lattice image (phase contrast image) of the parts indicated in Fig. 4 (d) by a yellow square with the zone axis parallel to  $[1\ 1\ 0]$ . (b) Fast Fourier transformed image of (a). Reciprocal spots corresponding to matrix (M) and twins (T) of an FCC structure is also indicated in the figure.

the tensile axis orientation of grains with type C and C + T at an applied strain of  $e \sim 5\%$ . Compared to the case of the CG specimen (Fig. 6 (a)), no obvious orientation dependence of deformation microstructure evolution was found. At a nominal strain of  $e \sim 15\%$ , the density of dislocations, stacking faults, and deformation twins further increased (Fig. 4 (e)). It is worth noting that many of the deformation twins observed in the UFG specimen were aligned nearly parallel to the tensile direction. This suggests that the Schmid factor on the twinning plane was very small compared to those in the CG specimen, which were mainly located along the planes inclined at  $45^\circ$  to the tensile axis. Also, only one variant of deformation twins was observed, and the deformation twins are localized (bundled) at some parts of grains in the UFG specimen. The implications of this finding will be discussed later.

### 3.3.3. Dislocation density and planar fault probability in the CG and UFG specimens

The representative diffraction profiles of the CG and UFG specimens obtained by in-situ XRD measurements during tensile deformation are presented in Fig. 7 (a) and (b), respectively. It can be easily found that with increasing strains, all the peaks broadened due to the increase in the density of lattice defects. Besides, the peak shape of  $\{1\ 1\ 1\}$  and  $\{2\ 0\ 0\}$  became asymmetric (tail of  $\{1\ 1\ 1\}$  and  $\{2\ 0\ 0\}$  peaks expanded toward higher and lower angle side, respectively). This is attributed to the increase in intrinsic stacking faults on  $\{1\ 1\ 1\}$  planes of FCC structures [29,30]. By fitting the peaks with physical models, it is possible to quantify the dislocation densities and planar faults probabilities of crystalline specimens based on the change in the peak shape. In Fig. 8 (a) and (b), dislocation densities and planar faults probabilities of the specimens evaluated by the CMWP method on the diffraction profiles in

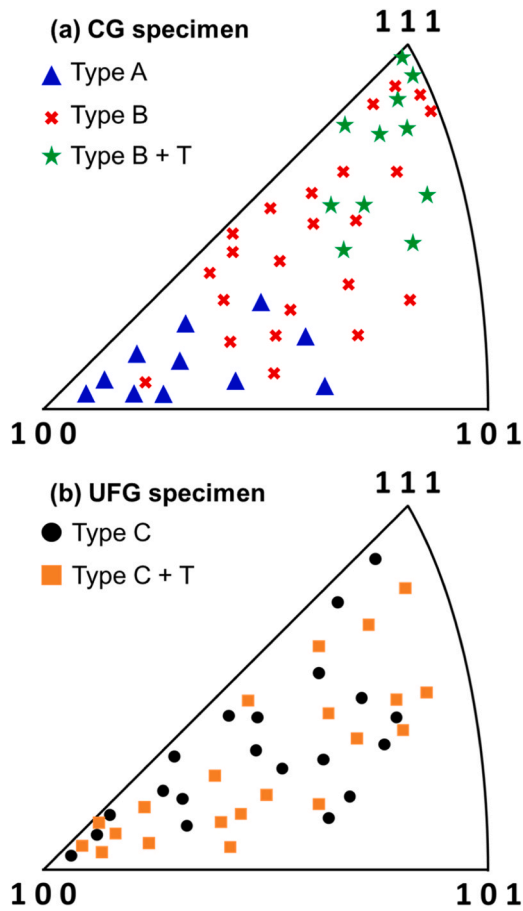


**Fig. 6.** Tensile axis orientations of grains with each deformation microstructure type in the (a) CG (Type A (blue triangles), B (red crosses), B + T (green stars)) and (b) UFG specimens (Type C (black circles), C + T (orange squares)) deformed to a strain of  $e \sim 5\%$ .

Fig. 7 are given. It was revealed that, compared to the CG specimen, both dislocation densities and planar fault probabilities of the UFG specimen increased more rapidly during tensile deformation. Particularly, the increasing rate of dislocation density of the UFG specimen at the initial stage of deformation was much higher than that in the CG specimen, similar to the previous reports on a high Mn steel [12]. Immediately before necking started, the dislocation densities of the CG and UFG specimens reached  $8.75 \times 10^{14} \text{ m}^{-2}$  (at a nominal strain of  $e \sim 0.42$ ) and  $8.53 \times 10^{14} \text{ m}^{-2}$  (at a nominal strain of  $e \sim 0.17$ ), respectively. The planar fault probabilities (abundance of intrinsic stacking faults) of the CG specimen started increasing at a nominal strain of  $e \sim 0.12$ , while those of the UFG specimen started increasing rapidly at a nominal strain of  $e \sim 0.04$ , where the inflection of work-hardening rate was observed in Fig. 2 (b).

## 4. Discussion

### 4.1. Deformation mechanisms of the CG specimen

In the CG specimen, DCs mainly appeared in grains that were oriented closely parallel to  $\langle 1\ 0\ 0 \rangle$ , classified as Type A. On the other hand, PDSs or Type B were more frequently observed in grains of other orientations. Furthermore, deformation twins were primarily seen in grains oriented approximately parallel to  $\langle 1\ 1\ 1 \rangle$ , referred to as Type B + T. This deformation microstructure evolution is similar to what has been observed in other polycrystalline FCC alloys with low SFE [31–33], as well as in the single crystal specimens with similar crystallographic orientations [24,34]. In grains with TA  $\sim // \langle 1\ 0\ 0 \rangle$ , the presence of

eight slip systems that have comparable Schmid factors enables the activation of these slip systems, leading to easy cross-slip for screw dislocations and the subsequent formation of DCs [33,35,36]. Conversely, the primary slip system, along with a few other systems with relatively higher Schmid factors, becomes active in grains of other orientations. In these orientations, due to the characteristics of high-alloy systems like HEAs and MEAs, the cross-slip of screw dislocations and dynamic recovery (annihilation of dislocations through cross slip during deformation) is more suppressed, not solely because of low SFE, compared to conventional low SFE FCC metals and alloys. Since the yield strength of high-alloy systems is significantly high owing to massive solution strengthening, the high flow stress mechanically expands the stacking faults on the primary plane due to the difference in shear stress acting on the Shockley partials [33,37]. Additionally, in all the grain orientations, the chemical interactions between alloying elements, often referred to as solute-solute or element-element interactions [38,39] and characteristic shape of stacking faults [40], further increase the activation energy required for cross-slip in any orientation. Consequently, the dislocation density in HEAs/MEAs with FCC structures increases more rapidly compared to conventional FCC metals and alloys [33]. The nucleation of deformation twins is more likely to occur in grains oriented closely parallel to  $\langle 1\ 1\ 1 \rangle$ , as the suppression of cross-slip of screw dislocations on the primary plane is most pronounced in this orientation in general. Also, the mechanisms mentioned above can further assist the suppression of cross-slip in high-alloy FCC materials. This can facilitate dislocation reactions that lead to the formation of twin nuclei, in line with the Miura-Narita-Takamura model [41], for instance. Overall, the deformation microstructures in the CG specimen followed the general tendency of FCC high-alloy systems with low SFE.

### 4.2. Deformation mechanisms of the UFG specimen

In contrast, the deformation microstructures in the UFG specimen primarily consist of tangled dislocations and widely-extended stacking faults, regardless of grain orientations. This can be due to the constraining effects exerted by grain boundaries. Previous studies [42] have categorized deformation microstructures in tensile-deformed pure Al with coarse grain sizes into three distinct types based on the TA of grains: (Type I) extended and straight dislocation boundaries along  $\{1\ 1\ 1\}$  planes; (Type II) oriented dislocation cell boundaries defining a three-dimensional cell structure; (Type III) a structure similar to (I) but the extended boundaries deviate from  $\{1\ 1\ 1\}$  planes. Further investigations [43] into the deformation microstructures of tensile-deformed Al with different mean grain sizes revealed that materials with a mean grain size of less than several micrometers uniformly exhibited DCs and tangled dislocations, independent of grain orientation. This indicates that near grain boundaries in polycrystals, the stress state is no longer uniaxial but complex due to the constraint by grain boundaries. As a result, the number of activated slip systems and density of dislocations near grain boundaries locally increases to maintain deformation compatibility with adjacent grains across grain boundaries. Since the density of grain boundaries is much higher in UFG materials compared to CG counterparts, dislocation density in UFG materials can increase more rapidly [12], and dislocations have more opportunities to interact with others from different slip systems and with grain boundaries [43], leading to a more uniform evolution of deformation microstructure compared to coarse-grained materials. Although the present MEA specimens exhibited higher density of stacking faults and deformation twins, as well as dislocations, the idea in the case of pure Al that mechanical constraint imposed by grain boundaries can result in more homogeneous plastic deformation and less orientation dependence of deformation microstructure evolution must be common. Thus, such influences of grain boundary constraints are considered to affect the deformation microstructure evolution and the resultant work-hardening behavior observed in the UFG specimen of the CoCrNi

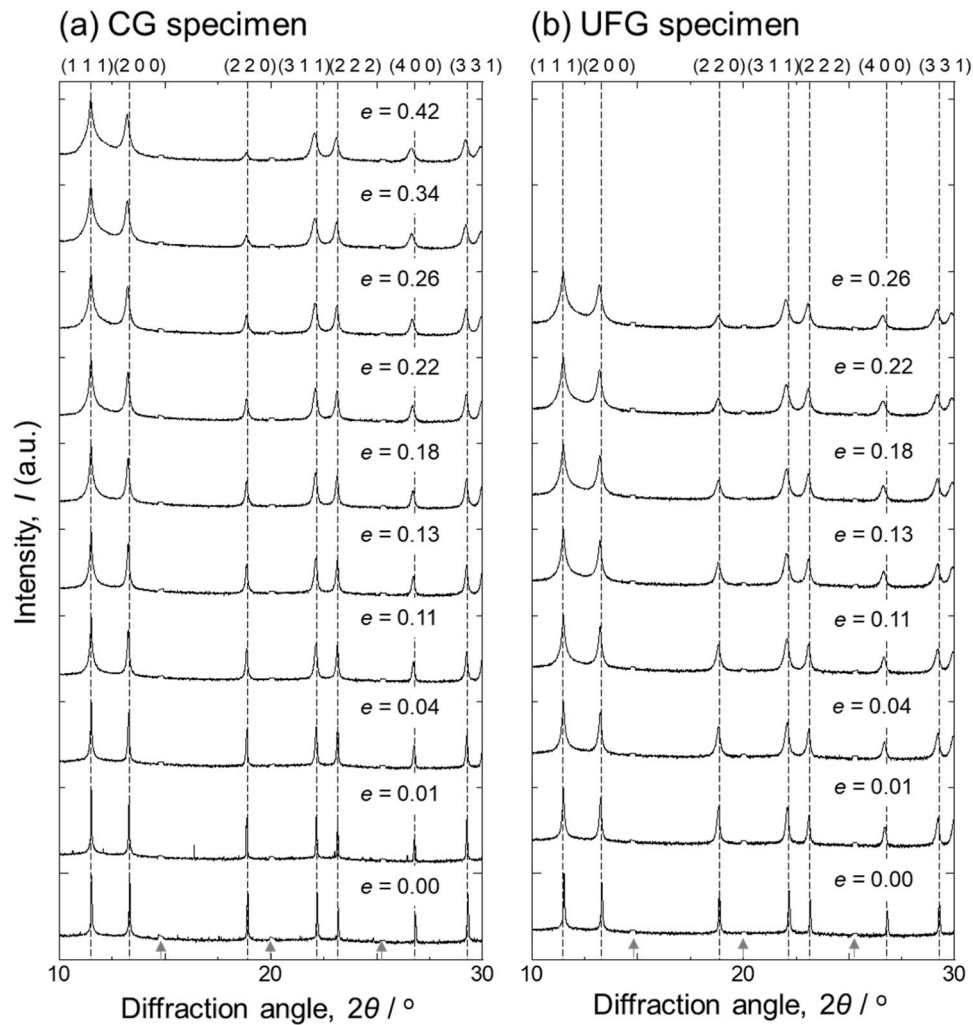


**Fig. 7.** XRD profiles of (a) CG and (b) UFG specimens obtained by in-situ measurements during tensile deformation. The vertical axis is the logarithmic scale so that the changes in the peak shapes can be easily distinguished. The corresponding indices of each peak for an FCC structure are also indicated in the figure. The parts pointed by gray arrows in the profiles for  $e = 0.00$  are the artifact intensity, without any physical meaning, caused by the X-ray detectors.

MEA and responsible for the disappearance of the orientation dependence.

Another characteristic of the deformation microstructure in the UFG specimen is the presence of widely extended stacking faults. Similar behavior has also been reported in some Cu-alloys [15]. Although the reason for the formation of such widely extended stacking faults is unclear, it may be related to the activation of multiple slip systems as well as the low SFE of the MEA. In the case of the UFG specimens, due to the constraint imposed by grain boundaries, a larger number of slip systems can be activated compared to the CG specimens, as discussed above. As a result of mechanical interactions among dislocations, in some cases, large shear stress can act on the leading partial dislocations, causing the stacking faults to expand widely. Another possibility is the influence of neighboring grains. If there is a grain where deformation state is very different from others, it can cause stress fields in neighboring grains. Such stress fields may also contribute to the expansion of stacking faults. In the case of UFG materials, owing to the high density of grain boundaries, more grains can be mechanically influenced by neighboring grains compared to CG materials. Thus, the presence of widely-extended stacking faults can be a nature of low SFE FCC materials with UFG microstructures.

Deformation twins have also been observed in the UFG specimen regardless of grain orientation. This is in contrast to the CG specimen, where deformation twins mainly form on primary or conjugate planes

with high Schmid factors. In the UFG specimen, many deformation twins tend to form on planes that are nearly parallel to the tensile axis of grains, which have a notably low Schmid factor. This difference indicates that the nucleation mechanism for deformation twins in the UFG specimen is fundamentally different from that in the CG specimen, suggesting that grain boundaries play a crucial role in the UFG specimen. Although the exact mechanisms are still unclear, the *Plaston* concept proposed by Tsuji et al. [18] offers a compelling explanation. It suggests that the nucleation of lattice defects, including dislocations, deformation twins, and deformation-induced martensite, arises from the collective motion of mechanically excited atoms at stress concentration points, such as special character grain boundaries and triple junctions. This hypothesis is supported by the observations of Hung et al. [44], reporting that the formation of deformation twins from specific grain boundaries with special characters, such as boundaries with large free volumes and partially incoherent  $\Sigma 3$  twin boundaries, during plastic deformation of a high-Mn steel in in-situ TEM studies and corroborated these findings with molecular dynamics simulations. They noted that the deformation twins also formed on lattice planes with low Schmid factors. In UFG polycrystals, the significantly higher density of grain boundaries, compared to conventional CG polycrystals, introduces a greater diversity in grain boundary character and increases the likelihood of adjacent grains being adjacent to special grain boundaries that are conducive to twin nucleation, as observed by Hung et al. Also, local

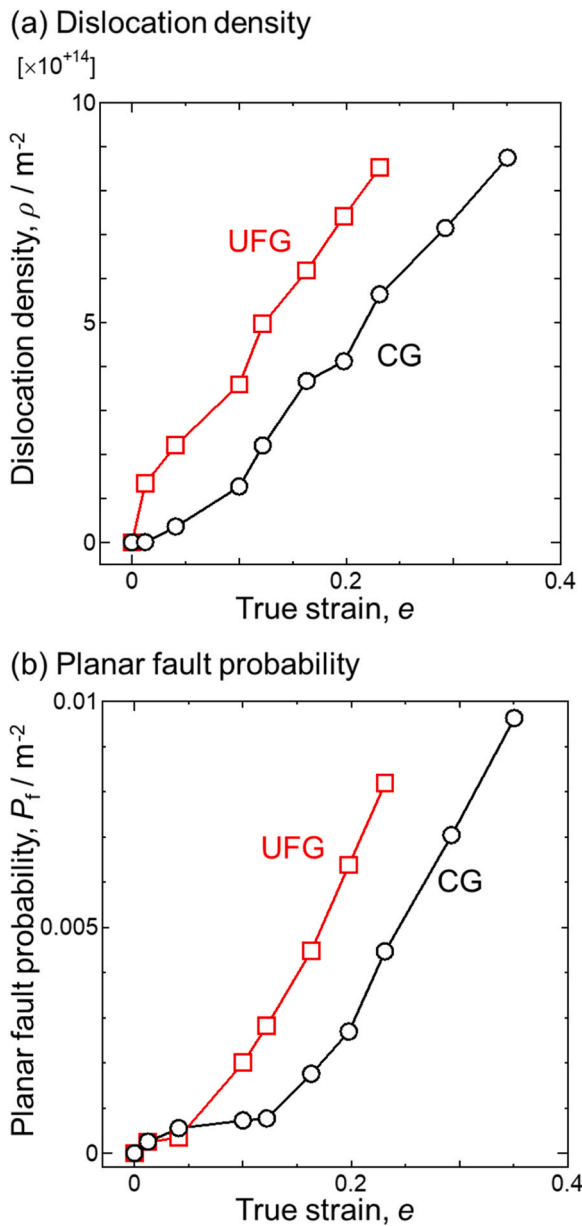


Fig. 8. (a) Dislocation density evolution and (b) planar fault probability evolution during tensile deformation quantified by the CMWP method based on the diffraction profiles in Fig. 7.

stress concentration near grain boundaries can further assist nucleation of deformation twins with such abnormal nucleation mechanisms, as suggested by the recent study by Park et al. [45] on stress distribution visualization near grain boundaries in polycrystals. Additionally, the lack of mobile dislocations, an important characteristic of UFG materials, can play a significant role. In order to activate the abnormal twinning mechanisms, the activity of other deformation modes like dislocation slip must be suppressed. Since we did not find traces of dislocation reactions near deformation twins in the UFG specimens, possibly such twin nucleation with abnormal mechanisms might be operated due to the lack of mobile dislocations in the grains as well as stress concentration near the grain boundaries with special characters.

Above all, we think that the following points can be common for the MEA and conventional low SFE FCC materials with UFG microstructures:

- (1) Due to the constraint imposed by grain boundaries and stress concentration in UFG materials, a larger number of slip systems can be activated resulting in more homogeneous plastic deformation (less orientation dependence of deformation microstructure evolution) and rapid increase in dislocation density compared to CG materials.
- (2) Due to the lack of mobile dislocations and stress concentration at grain boundaries in UFG materials, deformation twinning nucleated by a mechanism different from CG materials is more likely to happen.

Adding to these, inhibited dynamic recovery in the MEA (as discussed above) might further increase the density of dislocations and stacking faults as well as deformation twins nucleated by unconventional mechanisms.

#### 4.3. Strengthening and work-hardening mechanisms in the CG and UFG specimens

To gain further insight into the flow behavior of the CG and UFG specimens, Fig. 9 depicts their flow stress values ( $\sigma$ ) as a function of the square root of dislocation densities ( $\sqrt{\rho}$ ), which were quantified through the in-situ synchrotron XRD. The linear relationship observed in Fig. 9 suggests that the flow behavior of the CG and UFG specimens can be attributed to the increase in dislocation density, in accordance with the Bailey-Hirsch model, which is expressed as follows:

$$\sigma = \sigma_Y + M\alpha\mu b\sqrt{\rho}, \quad (2)$$

where  $\sigma_Y$  is the yield strength of materials,  $M$  is the Taylor factor ( $= 3.06$  for random texture),  $\alpha$  is the material constant (0.32 and 0.30 were obtained for the CG and UFG specimens, respectively),  $\mu$  is the shear modulus (91 GPa for CoCrNi MEA [26]), and  $b$  is the Burgers vector of perfect dislocations (estimated as 0.2520 nm for the CoCrNi MEA based on the in-situ synchrotron XRD measurements). Based on the results, the remarkable work-hardening capacity of the UFG specimen, which enables an excellent strength-ductility balance compared to conventional UFG metals, can be mainly attributed to the rapid increase in dislocation density, as shown in Fig. 8(a). Compared to conventional UFG metals [46,47], the increment of dislocation density in the MEA was significantly higher, resulting in an enhanced work-hardening rate and better strength-ductility balance. The rapid increase in dislocation density can be explained by inhibited dynamic recovery in the MEA than in other FCC metals. This is primarily because of the low SFE of the MEA, making dislocations difficult to cross slip during deformation. Moreover, our recent experimental work [33] suggested that, compared to conventional materials, dynamic recovery in FCC HEAs/MEAs can be more

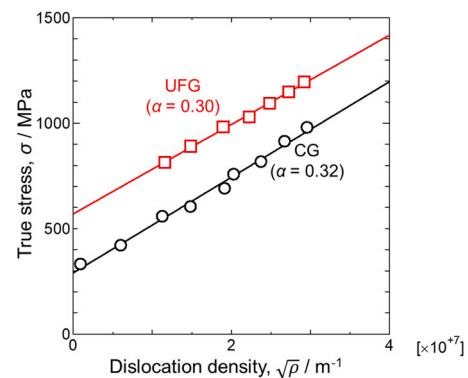


Fig. 9. Relationship between the flow stress and square root of dislocation densities in the CG and UFG specimens. The solid lines in the figure are fitting lines obtained by fitting the data points by Eq. (2). The corresponding  $\alpha$  values are also indicated together.

suppressed by their chemical heterogeneity in an atomic scale (different elements with different sizes occupy different lattice sites) which can increase the energy barrier for cross slip of screw dislocations, as discussed in the previous section.

The introduction of planar defects, such as stacking faults and deformation twins, which are commonly observed in low SFE FCC materials, can further reduce the mean free path of dislocations, thereby contributing to work-hardening via the dynamic Hall-Petch effect, although quantifying this contribution is challenging due to the lack of established theoretical frameworks. This effect of dynamic Hall-Petch mechanism could be more pronounced in the CG specimen because, compared to the UFG specimen, deformation twins are uniformly distributed, and multiple variants of twins are very effective to block dislocations of different slip systems during deformation [48]. This might be why the CG specimen showed higher work-hardening rate than the UFG specimen, as shown in Fig. 2 (b). Furthermore, deformation twinning introduces domains with orientations different from the matrix, resulting in the accumulation of a large number of geometrically necessary dislocations near twin boundaries to maintain the continuity of deformation across twin boundaries. This phenomenon is similar to the behavior observed at general high-angle grain boundaries, as discussed above. Consequently, the presence of planar faults can lead to a further increase in dislocation density locally. Also, according to previous literature [49,50], the emission of deformation twins as well as dislocations near crack tips can contribute to the retardation of fracture after necking. Although this is beyond the scope of our investigation, similar mechanisms might operate in the present materials as well.

In conclusion, the UFG specimen of the MEA have achieved an excellent strength-ductility balance compared to conventional UFG metals, primarily due to the evolution of unique deformation microstructures and the rapid increase in dislocation density, which can be largely attributed by inhibited dynamic recovery in the MEA. We believe that the insights gained here can be universally applicable to other low SFE FCC high-alloy systems with UFG microstructures, such as other FCC HEAs/MEAs [10,13,20], high-Mn steels [9,12], and Cu-alloys [14,15], which also exhibit an excellent strength-ductility balance.

## 5. Conclusions

In this study, we successfully fabricated a CoCrNi MEA with two different microstructures - fully recrystallized CG and UFG - using HPT and subsequent annealing. We investigated the deformation behaviors of specimens with both microstructures at room temperature, with a focus on the evolution of the deformation microstructures. Our aim was to clarify the characteristics of deformation microstructures in the UFG specimen compared to the CG specimen and to elucidate the microstructural origins of the excellent work-hardening capability observed in the UFG specimen compared to conventional UFG metals. The following points are the main findings of the present study.

- (1) The CG specimen exhibited a yield strength of 240 MPa, an ultimate tensile strength of 710 MPa, a uniform elongation of 43 %, and a total elongation of 58 %. While the UFG specimen showed a yield strength of 760 MPa, an ultimate tensile strength of 950 MPa, a uniform elongation of 17 %, and a total elongation of 33 %, which were consistent with previous reports.
- (2) In the CG specimen, the deformation microstructures varied depending on the TA of each grain, developing DCs, PDSs, and PDSs with deformation twins of multiple variants, similar to behaviors reported for the single crystal specimens. This behavior was also consistent with the previous literature on other FCC high-alloy systems.
- (3) In contrast, the UFG specimen exhibited tangled dislocations, extensive stacking faults, and nano-sized deformation twins of single variant regardless of grain orientations.
- (4) Interestingly, many deformation twins in the UFG specimen were found on lattice planes nearly parallel to the TA where the Schmid factor is notably low. This indicates a distinctive nucleation mechanism from that in the CG specimen. We discussed the observed differences in microstructural evolution between the CG and UFG specimens in light of grain boundary constraints.
- (5) Dislocation densities and planar faults probability quantified by our in-situ synchrotron XRD measurements during tensile deformation were higher in the UFG specimen than those in the CG specimen and in conventional UFG metals.
- (6) The relationship between the flow stress and dislocation densities of the CG and UFG specimens followed the Bailey-Hirsch model, suggesting that the work-hardening behavior of the specimens were primarily controlled by increases in the dislocation density and can be attributed to inhibited dynamic recovery in the MEA. The effect of planar faults which can dynamically reduce the mean free path of dislocations was also discussed and could be more pronounced in the CG specimen.

We concluded that the exceptional work-hardening ability of the UFG specimen of the CoCrNi MEA was attributed to the inhibited dynamic recovery (one of the characteristics of FCC high-alloy systems) and the formation of unique deformation microstructures, characterized by a high density of dislocations of different slip systems interacting frequently, and deformation twins nucleated through an unconventional mechanism, collectively contributing to retardation of plastic instability and realizing excellent strength-ductility balance.

## CRediT authorship contribution statement

**Nobuhiro Tsuji:** Writing – review & editing, Supervision, Resources, Project administration, Funding acquisition, Conceptualization. **Akinobu Shibata:** Writing – review & editing, Supervision. **Yu Bai:** Writing – review & editing, Supervision. **Takuto Ikeuchi:** Investigation, Formal analysis, Data curation. **Genki Yamashita:** Investigation, Formal analysis, Data curation. **Shuhei Yoshida:** Writing – original draft, Visualization, Validation, Methodology, Investigation, Funding acquisition, Formal analysis, Data curation, Conceptualization.

## Declaration of Competing Interest

The authors declare that they have no known competing financial interests or personal relationships that could have appeared to influence the work reported in this paper.

## Acknowledgments

This work was financially supported by the Elements Strategy Initiative for Structural Materials (ESISM), Japan Science and Technology Agency (JST) CREST (JPMJCR1994), Japan Society for the Promotion of Science (JSPS) the Fund for the Promotion of Joint International Research (International Leading Research) (No. JP23K20037), the Grant-in-Aid for Scientific Research on Innovative Area "High Entropy Alloys" (No. JP18H05455), the Grant-in-Aid for Scientific Research (S) (No. JP15H05767), the Grant-in-Aid for Early-Career Scientists (No. JP22K14501), the Grant-in-Aid for Research Activity Start-up (No. JP21K20487), and the Grant-in-Aid for JSPS Research Fellow (No. JP18J20766), all through the Ministry of Education, Culture, Sports, Science and Technology (MEXT), Japan. The synchrotron X-ray diffraction experiments were performed at the BL46XU of SPring-8 with the approval of the Japan Synchrotron Radiation Research Institute (JASRI) (Proposal No. 2019B1801). All the supports are gratefully appreciated.

## References

- [1] R.Z. Valiev, Y. Estrin, Z. Horita, T.G. Langdon, M.J. Zehetbauer, Y.T. Zhu, Fundamentals of superior properties in bulk NanoSPD materials, *Mater. Res Lett.* 3831 (2015) 1–21, <https://doi.org/10.1080/21663831.2015.1060543>.
- [2] R.Z. Valiev, M.J. Zehetbauer, Y. Estrin, H.W. Höppel, Y. Ivanisenko, H. Hahn, G. Wilde, H.J. Roven, X. Sauvage, T.G. Langdon, H.W. Höppel, Y. Ivanisenko, H. Hahn, G. Wilde, H.J. Roven, X. Sauvage, T.G. Langdon, The innovation potential of bulk nanostructured materials, *Adv. Eng. Mater.* 9 (2007) 527–533, <https://doi.org/10.1002/adem.200700078>.
- [3] N. Tsuji, Unique Mechanical properties of nanostructured metals, *J. Nanosci. Nanotechnol.* 7 (2007) 3765–3770, <https://doi.org/10.1166/jnn.2007.025>.
- [4] A. Azushima, R. Kopp, A. Korhonen, D.Y. Yang, F. Micari, G.D. Lahoti, P. Groche, J. Yanagimoto, N. Tsuji, A. Rosochowski, A. Yanagida, Severe plastic deformation (SPD) processes for metals, *CIRP Ann. Manuf. Technol.* 57 (2008) 716–735, <https://doi.org/10.1016/j.cirp.2008.09.005>.
- [5] R.Z. Valiev, Y. Estrin, Z. Horita, T.G. Langdon, M.J. Zehetbauer, Y. Zhu, Producing bulk ultrafine-grained materials by severe plastic deformation: ten years later, *Jom* 68 (2016) 1216–1226, <https://doi.org/10.1007/s11837-016-1820-6>.
- [6] K. Edalati, A. Bachmaier, V.A. Beloshenko, Y. Beygelzimer, V.D. Blank, W.J. Botta, K. Bryta, J. Cízek, S. Divinski, N.A. Enikeev, Y. Estrin, G. Faraji, R.B. Figueiredo, M. Fuji, T. Furuta, T. Grosdidier, J. Gubicza, A. Hohenwarter, Z. Horita, J. Huot, Y. Ikoma, M. Janeček, M. Kawasaki, P. Král, S. Kuramoto, T.G. Langdon, D. R. Leiva, V.I. Levitas, A. Mazilkin, M. Mito, H. Miyamoto, T. Nishizaki, R. Pippan, V.V. Popov, E.N. Popova, G. Purcek, O. Renk, Á. Révész, X. Sauvage, V. Sklenicka, V. Skrotzki, B.B. Straumal, S. Suwas, L.S. Toth, N. Tsuji, R.Z. Valiev, G. Wilde, M. J. Zehetbauer, X. Zhu, Nanomaterials by severe plastic deformation: review of historical developments and recent advances, *Mater. Res. Lett.* 10 (2022) 163–256, <https://doi.org/10.1080/21663831.2022.2029799>.
- [7] N. Tsuji, Y. Ito, Y. Saito, Y. Minamino, Strength and ductility of ultrafine grained aluminum and iron produced by ARB and annealing, *Scr. Mater.* 47 (2002) 893–899, [https://doi.org/10.1016/S1359-6462\(02\)00282-8](https://doi.org/10.1016/S1359-6462(02)00282-8).
- [8] M. Considère, L'emploi du fer de l'acier dans les constructions, *Memoire no 34, Ann. Des. Ponts Et. Chauss.-. ées 9* (1885) 574–775.
- [9] R. Saha, R. Ueji, N. Tsuji, Fully recrystallized nanostructure fabricated without severe plastic deformation in high-Mn austenitic steel, *Scr. Mater.* 68 (2013) 813–816, <https://doi.org/10.1016/j.scriptamat.2013.01.038>.
- [10] S.J. Sun, Y.Z. Tian, H.R. Lin, X.G. Dong, Y.H. Wang, Z.J. Zhang, Z.F. Zhang, Enhanced strength and ductility of bulk CoCrFeMnNi high entropy alloy having fully recrystallized ultrafine-grained structure, *Mater. Des.* 133 (2017) 122–127, <https://doi.org/10.1016/j.matdes.2017.07.054>.
- [11] S. Yoshida, T. Bhattacharjee, Y. Bai, N. Tsuji, Friction stress and Hall-Petch relationship in CoCrNi equi-atomic medium entropy alloy processed by severe plastic deformation and subsequent annealing, *Scr. Mater.* 134 (2017) 33–36, <https://doi.org/10.1016/j.scriptamat.2017.02.042>.
- [12] Y. Bai, H. Kitamura, S. Gao, Y. Tian, N. Park, M. heom Park, H. Adachi, A. Shibata, M. Sato, M. Murayama, N. Tsuji, Unique transition of yielding mechanism and unexpected activation of deformation twinning in ultrafine grained Fe-31Mn-3Al-3Si alloy, *Scientific Reports* 2021 11:1 11 (2021) 1–15, <https://doi.org/10.1038/s41598-021-94800-6>.
- [13] S.J. Sun, Y.Z. Tian, H.R. Lin, H.J. Yang, X.G. Dong, Y.H. Wang, Z.F. Zhang, Transition of twinning behavior in CoCrFeMnNi high entropy alloy with grain refinement, *Mater. Sci. Eng. A* 712 (2018) 603–607, <https://doi.org/10.1016/j.msea.2017.12.022>.
- [14] Y. Tian, A. Shibata, Z. Zhang, N. Tsuji, Ductility Sensitivity to Stacking Fault Energy and Grain Size in Cu–Al Alloys, *Mater. Res Lett.* 3831 (2016) 1–6, <https://doi.org/10.1080/21663831.2015.1136969>.
- [15] Y.Z. Tian, L.J. Zhao, S. Chen, A. Shibata, Z.F. Zhang, N. Tsuji, Significant contribution of stacking faults to the strain hardening behavior of Cu-15%Al alloy with different grain sizes, *Sci. Rep.* 5 (2015) 16707, <https://doi.org/10.1038/srep16707>.
- [16] R.Z. Valiev, N.A. Krasilnikov, N.K. Tsenev, Plastic deformation of alloys with submicron-grained structure, *Mater. Sci. Eng. A* 137 (1991) 35–40, [https://doi.org/10.1016/0921-5093\(91\)90316-F](https://doi.org/10.1016/0921-5093(91)90316-F).
- [17] R.B. Singh, N.K. Mukhopadhyay, G.V.S. Sastry, R. Manna, Recovery of ductility in ultrafine-grained low-carbon steel processed through equal-channel angular pressing followed by cold rolling and flash annealing, *Met. Mater. Trans. A Phys. Met. Mater. Sci.* 48 (2017) 1189–1203, <https://doi.org/10.1007/S11661-016-3892-X/FIGURES/9>.
- [18] N. Tsuji, S. Ogata, H. Inui, I. Tanaka, K. Kishida, S. Gao, W. Mao, Y. Bai, R. Zheng, J.-P. Du, Strategy for managing both high strength and large ductility in structural materials—sequential nucleation of different deformation modes based on a concept of plaston, *Scr. Mater.* 181 (2020) 35–42, <https://doi.org/10.1016/j.scriptamat.2020.02.001>.
- [19] H. Schreier, J.-J. Orteu, M.A. Sutton, Image Correlation for Shape, Motion and Deformation Measurements, Springer US, Boston, MA, 2009, <https://doi.org/10.1007/978-0-387-78747-3>.
- [20] S. Yoshida, T. Ikeuchi, T. Bhattacharjee, Y. Bai, A. Shibata, N. Tsuji, Effect of elemental combination on friction stress and Hall-Petch relationship in face-centered cubic high / medium entropy alloys, *Acta Mater.* 171 (2019) 201–215, <https://doi.org/10.1016/j.actamat.2019.04.017>.
- [21] A. Lavakumar, S. Yoshida, J. Punyafu, S. Ihara, Y. Chong, H. Saito, N. Tsuji, M. Murayama, Yield and flow properties of ultra-fine, fine, and coarse grain microstructures of FeCoNi equiatomic alloy at ambient and cryogenic temperatures, *Scr. Mater.* 230 (2023) 115392, <https://doi.org/10.1016/J.SCRIPMAT.2023.115392>.
- [22] G. Ribárik, Modeling of Diffraction Patterns Based on Microstructural Properties, Eötvös University Budapest, 2008.
- [23] G. Laplanche, A. Kostka, C. Reinhart, J. Hunfeld, G. Eggeler, E.P. George, Reasons for the superior mechanical properties of medium-entropy CrCoNi compared to high-entropy CrMnFeCoNi, *Acta Mater.* 128 (2017) 292–303, <https://doi.org/10.1016/j.actamat.2017.02.036>.
- [24] L. Li, Z. Chen, S. Kuroiwa, M. Ito, K. Kishida, H. Inui, E.P. George, Tensile and compressive plastic deformation behavior of medium-entropy Cr-Co-Ni single crystals from cryogenic to elevated temperatures, *Int. J. Plast.* (2021) 103144, <https://doi.org/10.1016/J.IJPLAS.2021.103144>.
- [25] Y.Z. Tian, S. Gao, L.J. Zhao, S. Lu, R. Pippan, Z.F. Zhang, N. Tsuji, Remarkable transitions of yield behavior and Lüders deformation in pure Cu by changing grain sizes, *Scr. Mater.* 142 (2018) 88–91, <https://doi.org/10.1016/j.scriptamat.2017.08.034>.
- [26] B. Yin, S. Yoshida, N. Tsuji, W.A. Curtin, Yield strength and misfit volumes of NiCoCr and implications for short-range-order, *Nat. Commun.* 11 (2020) 2507, <https://doi.org/10.1038/s41467-020-16083-1>.
- [27] N. Kamikawa, X. Huang, N. Tsuji, N. Hansen, Strengthening mechanisms in nanostructured high-purity aluminium deformed to high strain and annealed, *Acta Mater.* 57 (2009) 4198–4208, <https://doi.org/10.1016/j.actamat.2009.05.017>.
- [28] S. Gao, M. Chen, S. Chen, N. Kamikawa, A. Shibata, N. Tsuji, Yielding Behavior and Its Effect on Uniform Elongation of Fine Grained IF Steel, *Mater. Trans.* 55 (2014) 73–77, <https://doi.org/10.2320/matertrans.MA201317>.
- [29] M.S. Paterson, X-ray diffraction by face-centered cubic crystals with deformation faults, *J. Appl. Phys.* 23 (1952) 805–811, <https://doi.org/10.1063/1.1702312>.
- [30] J.M. Cowley, Diffraction by crystals with planar faults. I. General theory, *Urn:Issn: 0567-7394* 32 (1976) 83–87, <https://doi.org/10.1107/S0567739476000156>.
- [31] I. Gutierrez-Urrutia, D. Raabe, Multistage strain hardening through dislocation substructure and twinning in a high strength and ductile weight-reduced Fe–Mn–Al–C steel, *Acta Mater.* 60 (2012) 5791–5802, <https://doi.org/10.1016/j.actamat.2012.07.018>.
- [32] R. Ueji, N. Tsuchida, D. Terada, N. Tsuji, Y. Tanaka, A. Takemura, K. Kunishige, Tensile properties and twinning behavior of high manganese austenitic steel with fine-grained structure, *Scr. Mater.* 59 (2008) 963–966, <https://doi.org/10.1016/j.scriptamat.2008.06.050>.
- [33] S. Yoshida, R. Fu, W. Gong, T. Ikeuchi, Y. Bai, Z. Feng, G. Wu, A. Shibata, N. Hansen, X. Huang, N. Tsuji, Grain orientation dependence of deformation microstructure evolution and mechanical properties in face-centered cubic high/medium entropy alloys, *IOP Conf. Ser. Mater. Sci. Eng.* 1249 (2022) 012027, <https://doi.org/10.1088/1757-899X/1249/1/012027>.
- [34] B. Uzer, S. Picak, J. Liu, T. Jozaghi, D. Canadinc, I. Karaman, Y.I.I. Chumlyakov, I. Kireeva, On the mechanical response and microstructure evolution of NiCoCr single crystalline medium entropy alloys, *Mater. Res Lett.* 6 (2018) 442–449, <https://doi.org/10.1080/21663831.2018.1478331>.
- [35] X. Huang, G. Winther, Dislocation structures. Part I. Grain orientation dependence, *Philos. Mag.* 87 (2007) 5189–5214, <https://doi.org/10.1080/14786430701652851>.
- [36] G. Winther, X. Huang, Dislocation structures. Part II. Slip system dependence, *Philos. Mag.* 87 (2007) 5215–5235, <https://doi.org/10.1080/14786430701591505>.
- [37] S.M. Copley, B.H. Kear, The dependence of the width of a dissociated dislocation on dislocation velocity, *Acta Metall.* 16 (1968) 227–231, [https://doi.org/10.1016/0001-6160\(68\)90118-1](https://doi.org/10.1016/0001-6160(68)90118-1).
- [38] W.G. Nöhring, W.A. Curtin, Cross-slip of long dislocations in FCC solid solutions, *Acta Mater.* 158 (2018) 95–117, <https://doi.org/10.1016/j.actamat.2018.05.027>.
- [39] W.G. Nöhring, W.A. Curtin, Dislocation cross-slip in fcc solid solution alloys, *Acta Mater.* 128 (2017) 135–148, <https://doi.org/10.1016/j.actamat.2017.02.027>.
- [40] T.M. Smith, M.S. Hooshmand, B.D. Esser, F. Otto, D.W. McComb, E.P. George, M. Ghazisaeidi, M.J. Mills, Atomic-scale characterization and modeling of 60° dislocations in a high entropy alloy, *Acta Mater.* 110 (2016) 352–363, <https://doi.org/10.1016/j.actamat.2016.03.045>.
- [41] S. Miura, J. Takamura, N. Narita, Orientation dependence of the flow stress for twinning in silver crystals, *Trans. JIM* 9 (1968) 555.
- [42] X. Huang, N. Hansen, Grain orientation dependence of microstructure in aluminium deformed in tension, *Scr. Mater.* 37 (1997) 1–7, [https://doi.org/10.1016/S1359-6462\(97\)00072-9](https://doi.org/10.1016/S1359-6462(97)00072-9).
- [43] G.M. Le, A. Godfrey, N. Hansen, W. Liu, G. Winther, X. Huang, Influence of grain size in the near-micrometre regime on the deformation microstructure in aluminium, *Acta Mater.* 61 (2013) 7072–7086, <https://doi.org/10.1016/j.actamat.2013.07.046>.
- [44] C.-Y. Hung, T. Shimokawa, Y. Bai, N. Tsuji, M. Murayama, Investigating the dislocation reactions on  $\Sigma 3\{111\}$  twin boundary during deformation twin nucleation process in an ultrafine-grained high-manganese steel, *Scientific Reports* 2021 11:1 11 (2021) 1–13, <https://doi.org/10.1038/s41598-021-98875-z>.
- [45] M. heom Park, S. Yako, Y. Takeda, A. Shibata, N. Tsuji, Making stress visible: a method to quantify local stress distribution in metals using digital image correlation method, *Scr. Mater.* 252 (2024) 116265, <https://doi.org/10.1016/J.SCRIPMAT.2024.116265>.
- [46] H. Adachi, H. Mizowaki, M. Hirata, D. Okai, H. Nakanishi, Measurement of dislocation density change during tensile deformation in coarse-grained aluminum by in-situ XRD technique with tester oscillation, *Mater. Trans.* 62 (2021) 62–68, <https://doi.org/10.2320/MATERTRANS.L-M2020861>.
- [47] Y. Miyajima, S. Okubo, H. Abe, H. Okumura, T. Fujii, S. Onaka, M. Kato, Dislocation density of pure copper processed by accumulative roll bonding and equal-channel angular pressing, *Mater. Charact.* 104 (2015) 101–106, <https://doi.org/10.1016/J.MATCHAR.2015.04.009>.

- [48] M. Bönisch, Y. Wu, H. Sehitoglu, Hardening by slip-twin and twin-twin interactions in FeMnNiCoCr, *Acta Mater.* 153 (2018) 391–403, <https://doi.org/10.1016/j.actamat.2018.04.054>.
- [49] B. Gludovatz, A. Hohenwarter, K.V.S. Thurston, H. Bei, Z. Wu, E.P. George, R. O. Ritchie, Exceptional damage-tolerance of a medium-entropy alloy CrCoNi at cryogenic temperatures, *Nat. Commun.* 7 (2016) 10602, <https://doi.org/10.1038/ncomms10602>.
- [50] Z. Zhang, H. Sheng, Z. Wang, B. Gludovatz, Z. Zhang, E.P. George, Q. Yu, S.X. Mao, R.O. Ritchie, Dislocation mechanisms and 3D twin architectures generate exceptional strength-ductility-toughness combination in CrCoNi medium-entropy alloy, *Nat. Commun.* 8 (2017) 14390, <https://doi.org/10.1038/ncomms14390>.